Electronic Supplementary Material (ESI) for Journal of Materials Chemistry A.

Supplementary Materials for

Janus wood membranes for autonomous water transport and fog collection

Yong Ding, Kunkun Tu, Ingo Burgert, Tobias Keplinger*

Correspondence to: tkeplinger@ethz.ch

This PDF file includes:

Methods
Supplementary Text
Figure. S1 to S7
Table S1 to S2
Captions for Movies S1 to S3

Other Supplementary Materials for this manuscript include the following:

Movies S1 to S3

Methods

Fabrication of Janus wood membranes.

Native wood membrane: Norway spruce cross sections (thickness: 1.0 mm, 1.5 mm, 2.0 mm, 2.5 mm and 3.0 mm) were cut from large wood samples with similar growth ring patterns by a laser cutter (Trotec, Speedy 300) (Fig. S1). All samples were stored at 20 ^{o}C/65% relative humidity before treatment and characterization.

Hydrophobic wood membrane: The as-prepared wood membranes were modified with fluoro-oxysilane (1H,1H,2H,2H-Perfluorooctyltriethoxysilane, Sigma-Aldrich) and titanium oxide nanoparticles (TiO_2, <150 nm particle size, 40 wt.% dispersion in H_2O, Sigma-Aldrich) in ethanol solvent with vacuum for 3 hours under stirring at room temperature. The modified wood membranes were washed with ethanol several times until the solution was clear. Then samples were dried in a vacuum oven at 65 ^{o}C for 12 hours.

Janus wood membrane: The hydrophobic wood membrane was then irradiated under a UV lamp (UVACUBE 400, 400 W, sun simulated spectrum, 40 cm away from top surface) only on one side to create a wettability gradient through the thickness of the membrane.

Measurement of directional water transport property. Water transport performance of native wood membrane, hydrophobic membrane, and both sides of Janus wood membranes (horizontally and vertically oriented) were tested by blue-colored water droplets (50 µL, in which 50 mg/L of Reactive Blue 2) and recorded by camera.

Measurement of fog collection property and water evaporation rate. Fog capture device was constructed of a container sealed by wood membrane (10 × 10 mm^2).

Fog collection efficiency: Fog capture devices were placed vertically to test fog collection efficiency. The fog flow with a velocity of 70 cm s^{-1}, which is similar to natural fog speed, was generated by a commercial humidifier. The saturated fog, starting 10 cm away from the devices, was propelled horizontally toward the wood membrane. Every 10 min, the collected water in the container was weighed, and the collecting period lasted for 1 h. This

measurement was carried out in a climate room with the relative humidity and temperature maintained stably at 65%, and 25 ºC, respectively. The fog harvesting measurements were repeated for 10 cycles. The fog harvesting efficiency after each cycle was calculated by comparing with first measurement.

Water evaporation rate: The water evaporation rates of different devices at multiple temperatures were evaluated. Fog collection devices with water in the containers were placed in the thermostatic oven with constant air flow. The temperatures were set at 25 ºC, 45 ºC, and 65 ºC, and the weight loss caused by water evaporation were measured every 10 min.

Characterizations.

Water contact angle (CA) values were measured on a contact angle goniometer (DAS100). Water drop volume for the measurements was 10 μL in. All reported CA values represent the mean of five measurements.

Surface morphology and chemical composition of wood membranes were studied with a scanning electron microscope (SEM; FEI Quanta 200F, Hillsboro, OR, USA) equipped with energy dispersive X-ray spectroscopy (EDXS; Ametek-EDAX). Wood samples were coated with a sputter coater (CCU-010, Safematic, Switzerland). A Pt−Pd (80/20) coating of ~10 nm thickness was applied.

Compression tests and tensile tests were performed using a universal testing machine (Zwick Roell) equipped with a 10 kN load cell. Prior to the compression tests, ten specimens with the dimensions of 10 × 10 × 5 mm^3 (radial × tangential × longitudinal) were dried in an oven at 65 °C until constant mass. The testing speed was 0.5 mm min^{-1} and a preloading of 100 N was used. For the tensile tests, ten previously dried specimens with the dimensions 10 × 50 × 1.5 mm^3 (radial × tangential × longitudinal) were used with 40 mm initial length between two grips. The preload was set to 10 N and the displacement was measured with a travel sensor at a speed of 0.35 mm·min^{-1}. Both the compression and tensile tests were conducted at 20 °C and 65% relative humidity.

Supplementary Text

Morphology of saw-cutting wood cross section and laser-cutting wood cross section.

Figure S2 a shows the typical morphology of a saw cut wood cross-section. The surface roughness is non-uniform. There are three main types of morphology patterns. In region 1 (Fig. S2 d), the smooth and dense surface is formed by folded cell walls of latewood, which has thick cell walls and narrow lumina. Region 2 and 3 are earlywood parts (thin cell walls and larger lumina) with different morphologies. Region 2 (Fig. S2 b) is a partially open porous structure. Region 3 (Fig. S2 c) with high roughness is caused by folded cell wall fragments from shredded fibers. Hence, there is a large surface roughness distribution with samples prepared by saw cutting.

Roughness can have a profound effect on the shape and behavior of a liquid droplet on a solid surface. An homogeneous surface structure of the native wood membrane is a prerequisite to creating well-defined wettability gradients through the wood membrane. In this work, we used laser cutting to fabricate thin wood membranes with smooth surface on both sides instead of saw cutting. The samples prepared by laser cutting show a wood scaffold with all lumina open (**Fig. S3**). Compared to samples after saw cutting, the surface after laser cutting is uniform and the latewood and earlywood region are well preserved.

Mechanism of TiO_2 induced photocatalytic decomposition of fluoro-oxysilane

Under UV irradiation, TiO_2 nanoparticles were excited to generate electron–hole pairs. The holes reacted with surface-adsorbed water to generate oxygen and protons, whereas the electrons could be captured by fluoro-oxysilane, and lead to degradation of alkyl chain[1-4]. Detailed EDXS measurements and CA measurements are performed to confirm the removal of fluoro-oxysilane. Although EDXS is not a quantitative method, by our approach it allows for semi-quantitative analysis of the sample. The samples for EDXS measurements were first sputtered by Pt/Pd to increase the conductivity. The sum EDXS spectrum shows all detectable

element peaks. During the element analysis, we excluded the Pt and Pd from calculation and only normalized the relative content of elements of interest: C, O, Ti, Si, F. Therefore, the presence/disappearance of specific peaks can be used to determine the composition in a semi-quantitative way [5].

Compared with the spectrum of the unexposed side, the fluorine peak disappears which clearly confirms the degradation of silane under UV-light. The EDXS mapping measurements were repeated three times. In **Fig. S4** we displayed six EDXS mapping spectra of unexposed side and UV-irradiated side, respectively. Although the relative content of each element varies, the removal of fluorine is confirmed by all spectra. Furthermore, in contrast to the unexposed side, the CA of UV-irradiated side was decreased from 102.8° to 23.4°.

In addition, we carried out FTIR measurements. The spectra are shown in **Fig. S5** and the peaks are assigned according to literature [6, 7]: 1720 cm^{-1} –C=O (hemicellulose); 1650 cm^{-1} Ti-OH (bending) and C=O (cellulose); 1600 cm^{-1} aromatic (lignin); 1515 cm^{-1} aromatic (lignin); 1456 cm^{-1} OH (bending); 1423 cm^{-1} CH_2 (bending); 1375 cm^{-1} CH (bending) and Ti-O; 1246 cm^{-1} OH; 1153 cm^{-1} C-O-C (symmetric); 1030 cm^{-1} C-O (stretch). However, we didn't observe characteristic peaks of fluoro-oxysilane, which hinders a study of the UV-induced silane degradation. The reasons for the missing silane bands are: i) The amount of fluoro-oxysilane is very low (confirmed by the EDXS measurements in Fig. S4); ii) The characteristic peaks of fluoro-oxysilane overlap severely with those of wood substrates [8]: CF_2 (~1144cm^{-1} and ~1245 cm^{-1}); C-O-C (~1153cm^{-1}); OH (~1246cm^{-1}).

In conclusion, the repeatable and consistent results from the EDXS measurement and CA measurement confirmed the successful removal of fluoro-oxysilane and the wettability was converted from hydrophobicity to hydrophilicity.

Estimating the percentage of tracheids opened from both ends in wood cross section

When a wood cross section is cut, some tracheids might be opened from both ends, these tracheids let water directly flow through. Other tracheids might be closed from one end,

blocking the water. To estimate the percentage of tracheids opened from both ends in wood cross section, we reasoned on the basic scheme shown in **Fig. S6**. Tracheids length is denoted as d. To simplify our model, we make the following assumptions: i) all the tracheids have the same length, ii) they are aligned perpendicularly to the cross section, iii) they are randomly distributed in the vertical direction, iv) all bordered pits are closed, excluding transport from one tracheid to another. Starting with one single tracheid, we define the length of a tracheid d as 3 mm (d = 3), and x is the thickness of our wood membranes (Figure S4 b). With these parameters we can formulate the probability that a single tracheid is open as:

$$P(i) = \frac{\mathrm{d} - \mathrm{x}}{\mathrm{d}}$$

Using this equation, if x is set to 1.5, or 3 mm, then the probabilities to have a single tracheid open from both ends are respectively 0.5 and 0. The probability indicates that if we use a 1.5 mm thick wood cross section, the most probable scenario is that we obtain 50% of the tracheids open from both ends.

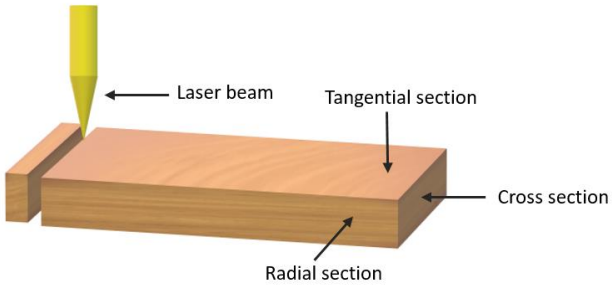

Fig. S1.
Scheme of preparing cross-section wood membranes by laser cutting.

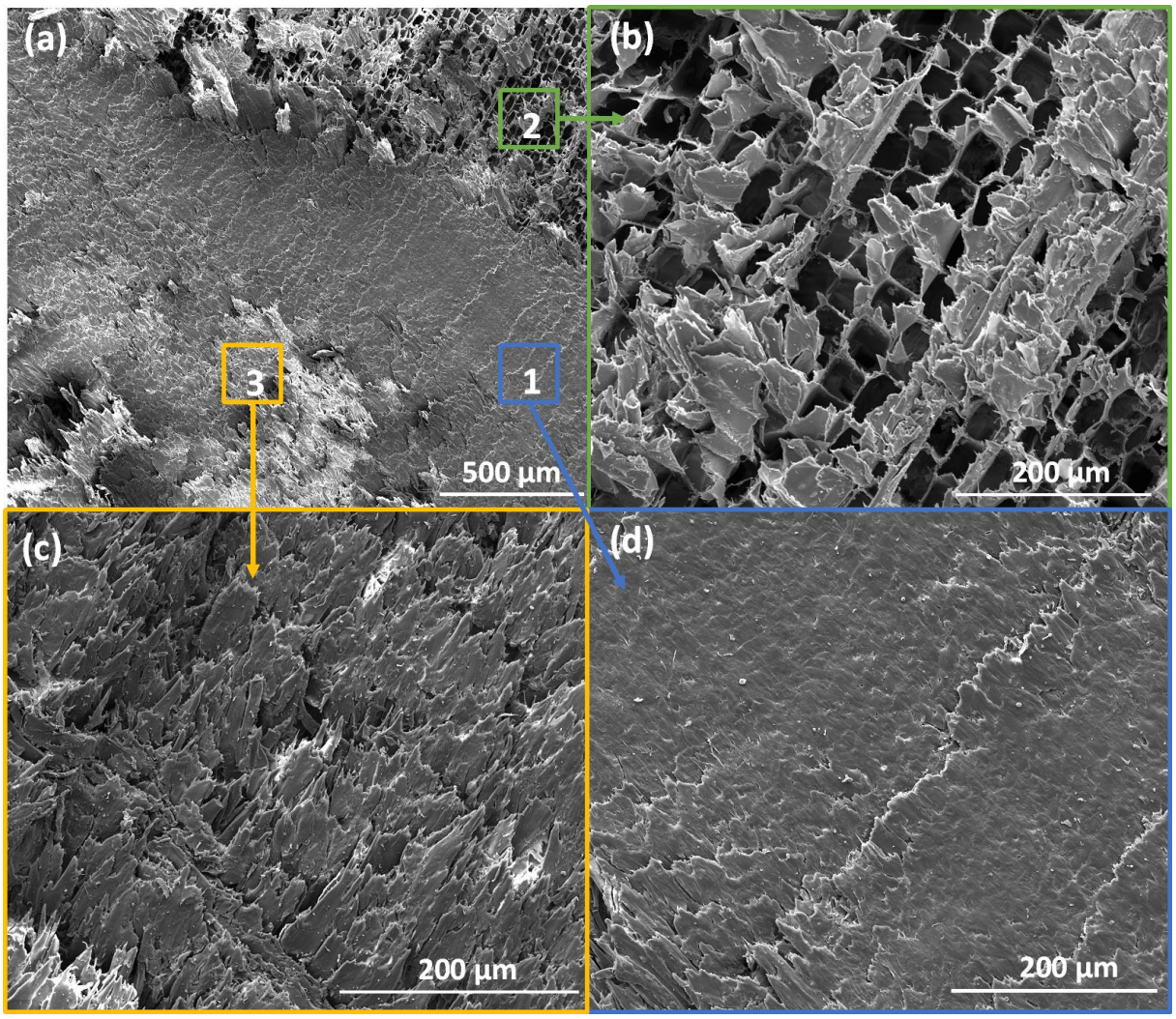

Fig. S2.
Morphology of saw-cut cross section of wood. (**a**) Overview of cross section. (**b** and **c**) Earlywood region. (**d**) Latewood region.

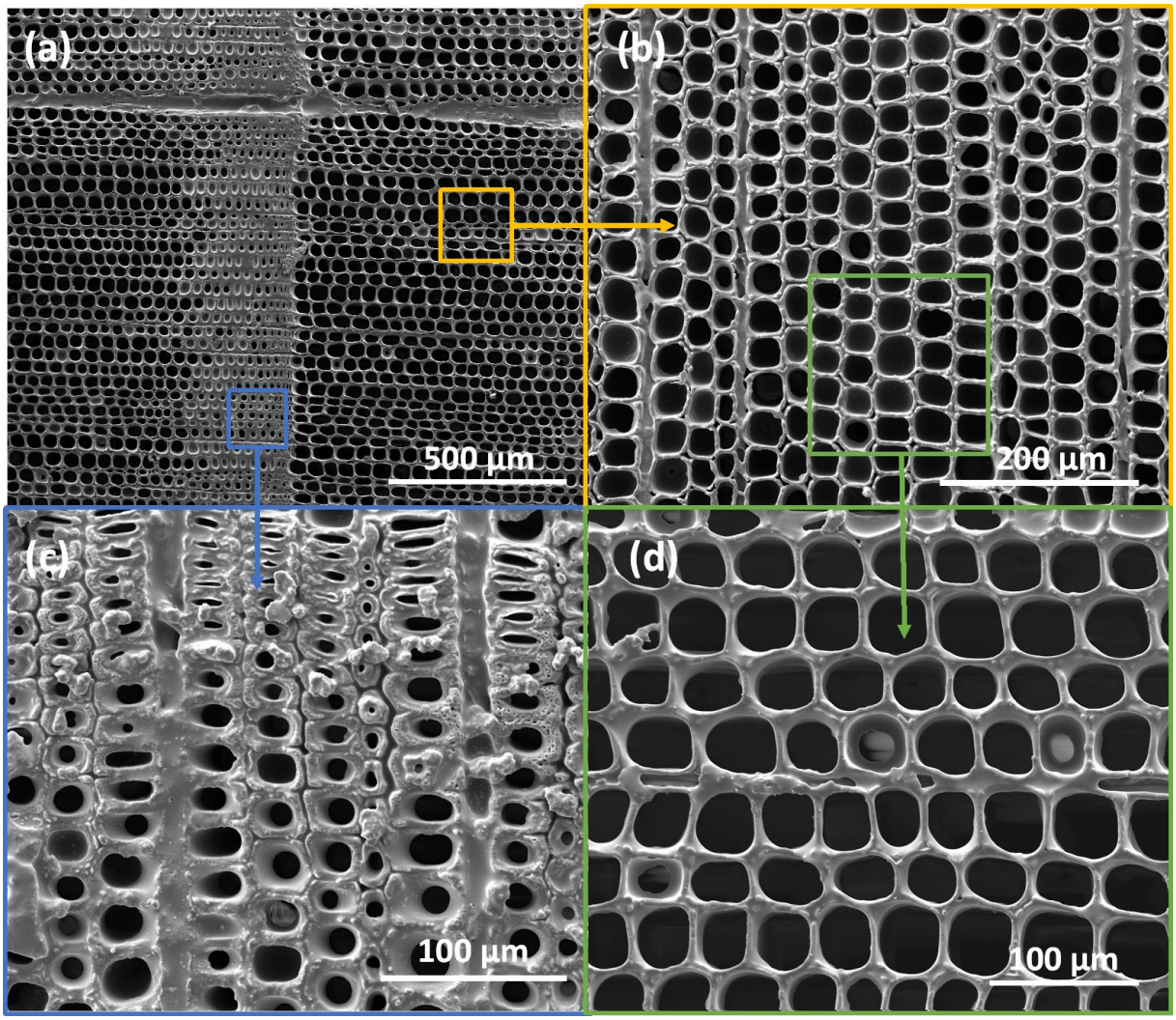

Fig. S3.
Morphology of the laser-cut cross section of wood. (**a**) Overview of the cross section. (**b** and **d**) Earlywood region. (**c**) Latewood region.

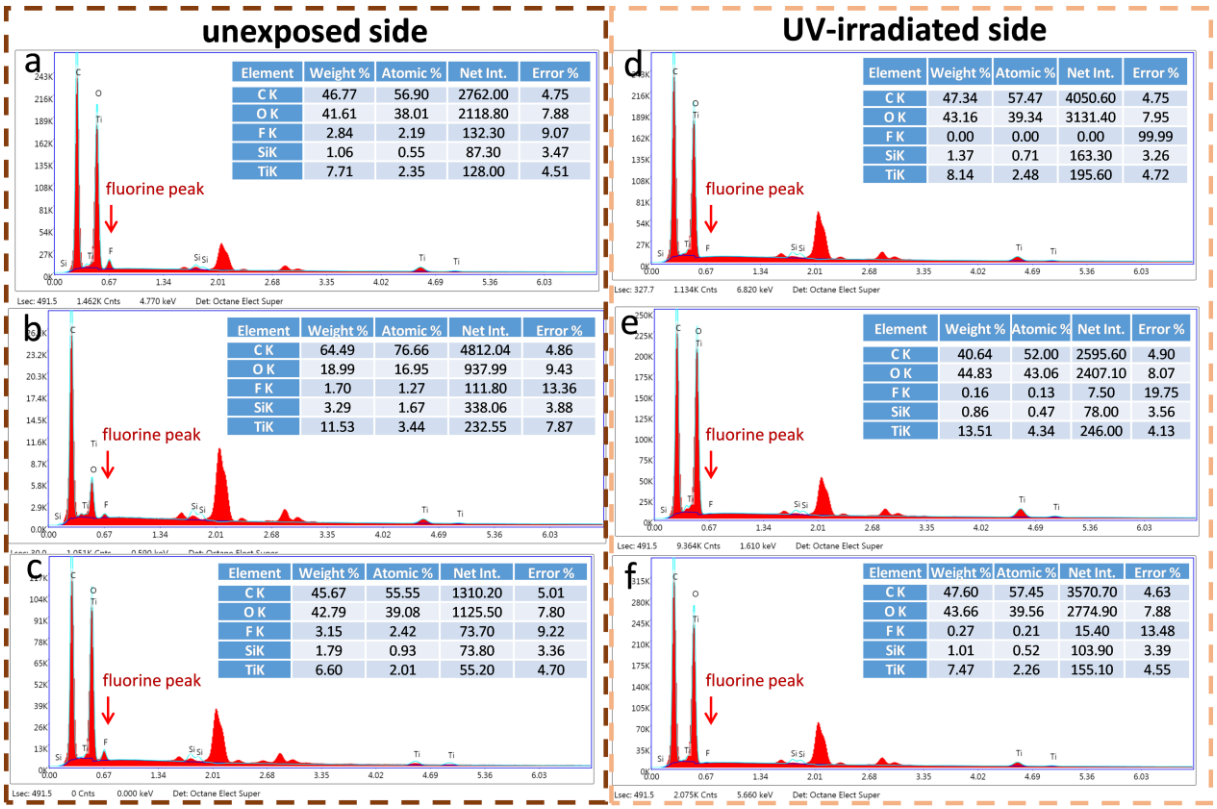

Fig. S4.
EDXS spectra of Janus wood membrane (**a-c**) unexposed side, (**d-f**) UV-irradiated side

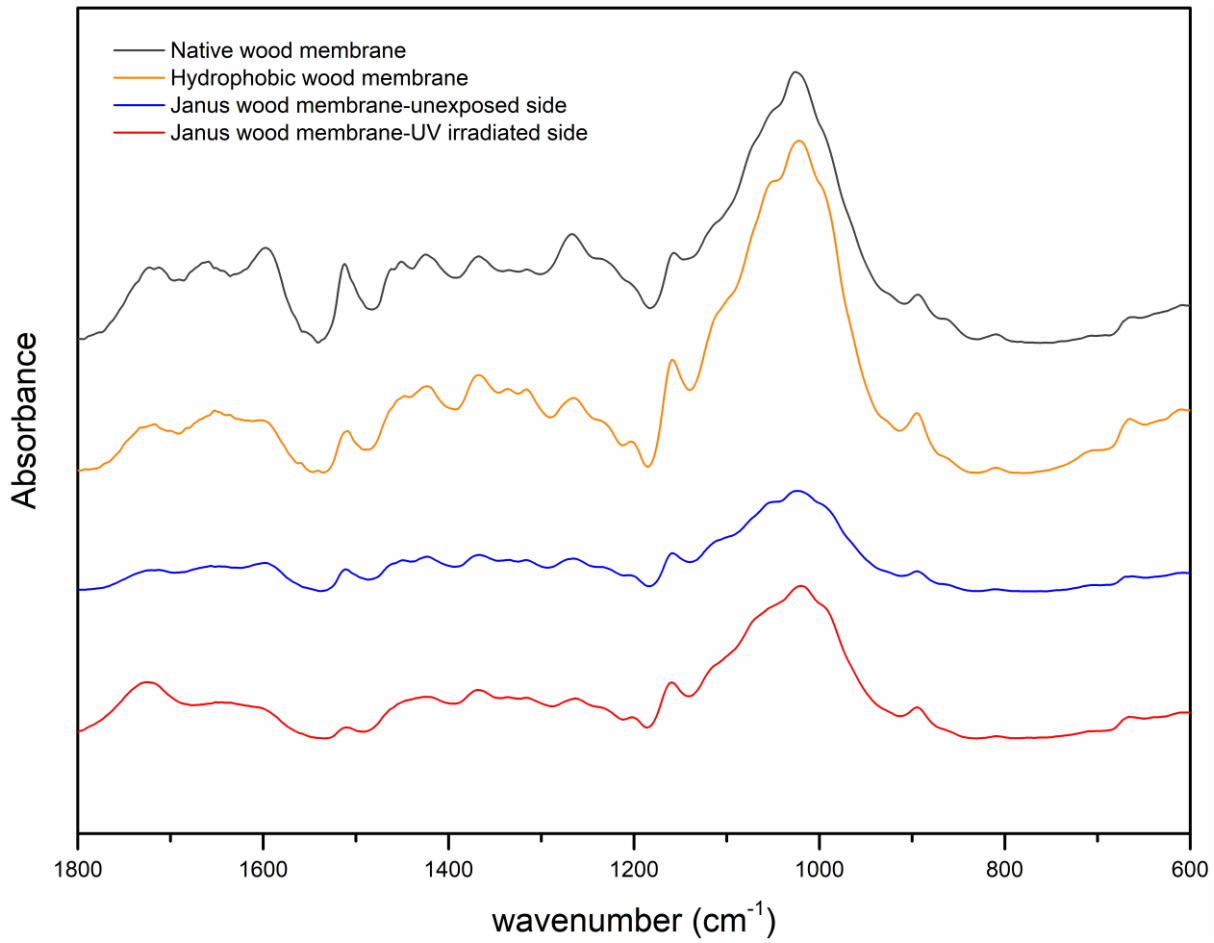

Fig. S5.
FTIR spectra of wood membranes

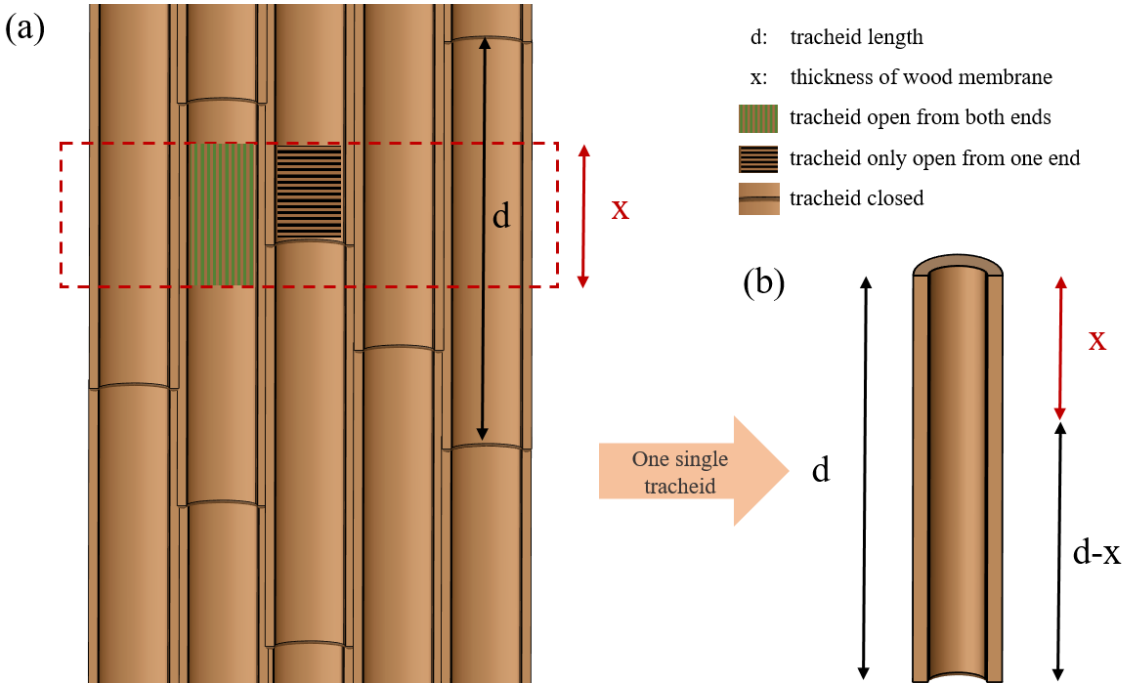

Figure S6.
a) Scheme of randomly distributed tracheids in spruce wood. The dotted red frame illustrates a wood membrane. The green tracheid would be open from both ends and the black tracheid would be only open from one end. b) Scheme of the parameters on a single tracheid. d is the length of tracheid, and x is the thickness of membrane.

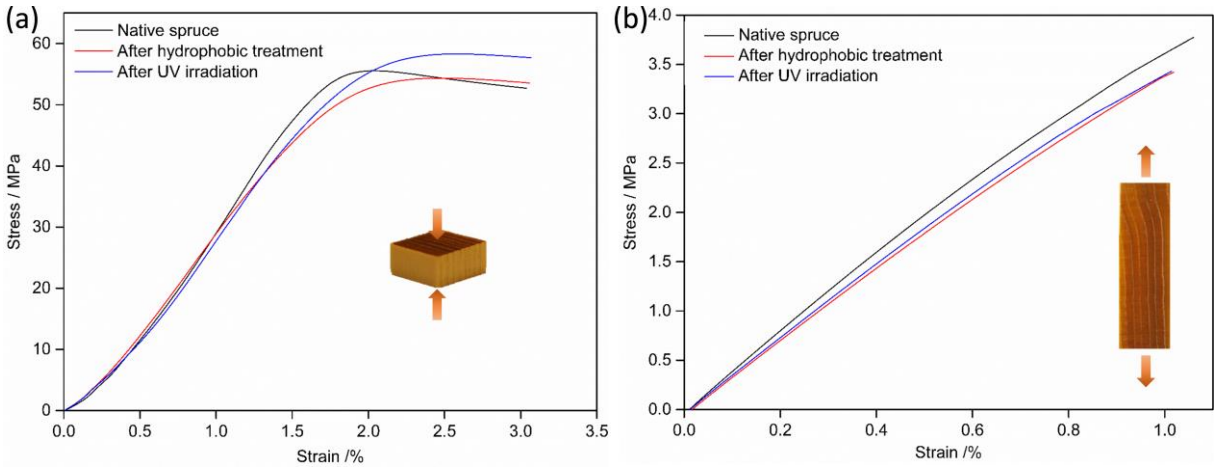

Fig. S7.

Mechanical performance. (**a**) Stress-strain curves of compressive tests. (**b**) Stress-strain curves of tensile tests.

Table S1 Comparison between Janus wood membrane and other substrates regarding their mechanical properties

	Janus wood membrane	Cotton fabric [9, 10]	PAN Nanofibrous membrane [11-14]
Compression strength (MPa)	58 (longitudinal direction)	/	/
Tensile strength (MPa)	3.4 (radial direction)	~10	0.2~2
Modulus of elasticity (MPa)	386 (radial direction)	10~150	50-75
Density (kg/m^3)	470	1500	1200

Table S2 Comparison between Janus wood membrane and other substrates regarding their cost-efficiency

		Janus wood membrane	Nanofibrous [15]	Cotton [5]
Raw materials	Matrix	Norway Spruce: abundant and renewable resource, 0.3 USD/kg **&**	Polyacrylonitrile: 5800 USD/kg *****	Cotton fabric:8 USD/kg **#**
	Additives	• TiO_2: 3 USD/g ***** • Perfluorooctyltriethoxysilane: 30 USD/g *****	• SiO_2: 2.6 USD/g *****	• Titanium tetraisopropoxide: 120 USD/L ***** • Hexadecyltrimethoxysilane: 280 USD/L ***** • Trimethoxysilylpropane thiol: 40 USD/g *****
Fabrication		➢ Vacuum impregnation ➢ UV irradiation	➢ Electrospun	➢ Dip coating ➢ UV irradiation
Application Set-up		Serves as both, structural material and functional section	Needs to be incorporated into a scaffold	Needs to be incorporated into a scaffold

Price information from: ***** Sigma Aldrich; **&** U.S. lumber and panel market report; **#** Amazon.com

Movie S1.

Water dropping on different wood membranes. 0 - 22 s: Water dropping on native wood membrane; water impermeable; 3 times accelerated. 23 - 26 s: Water dropping on hydrophobic wood membrane; water impermeable; 3 times accelerated. 47 - 67 s: Water dropping on Janus wood membrane; water transported, original speed.

Movie S2.

Water dropping on Janus wood membrane in different directions. 0 - 12 s: in positive direction; water transported; original speed. 13 - 26 s: in reverse direction; water blocked; 3 times accelerated.

Movie S3.

Anti-gravity transport of water on Janus wood membrane. 0 - 12 s: Water feeding upwards to a horizontally positioned Janus wood membrane in positive direction; water transported against gravity; original speed. 13 - 27 s: Water feeding upwards to a horizontally positioned Janus wood membrane in reverse direction, water blocked, 2 times accelerated. 28 - 48 s: Water feeding to a vertically positioned Janus wood membrane in positive direction, water transported, 2 times accelerated. 49 - 70 s: Water feeding to a vertically positioned Janus wood membrane in reverse direction, water blocked, 2 times accelerated.

References:

1. H. Bai, L. Wang, J. Ju, R. Sun, Y. Zheng and L. Jiang, *Adv. Mater.*, 2014, **26**, 5025-5030.
2. X. Zhang, H. Kono, Z. Liu, S. Nishimoto, D. A. Tryk, T. Murakami, H. Sakai, M. Abe and A. Fujishima, *Chem. Commun.*, 2007, DOI: 10.1039/b713432k, 4949-4951.
3. Y. Q. Zhu, J. F. Shi, Q. Z. Huang, L. L. Wang and G. Xu, *Chem. Commun.*, 2017, **53**, 2363-2366.

4. S. Nishimoto, M. Becchaku, Y. Kameshima, Y. Shirosaki, S. Hayakawa, A. Osaka and M. Miyake, *Thin Solid Films*, 2014, **558**, 221-226.
5. H. Wang, J. Ding, L. Dai, X. Wang and T. Lin, *J. Mater. Chem.*, 2010, **20**, 7938-7940.
6. A. Leon, P. Reuquen, C. Garin, R. Segura, P. Vargas, P. Zapata and P. A. Orihuela, *Appl Sci-Basel*, 2017, **7**.
7. N. Gierlinger, L. Goswami, M. Schmidt, I. Burgert, C. Coutand, T. Rogge and M. Schwanninger, *Biomacromolecules*, 2008, **9**, 2194-2201.
8. D. Devaprakasam, S. Sampath and S. K. Biswas, *Langmuir*, 2004, **20**, 1329-1334.
9. L. Hao, R. Wang, Y. Zhao, K. Fang and Y. J. C. Cai, 2018, **25**, 6759-6769.
10. M. Shibata, N. Teramoto, T. Nakamura and Y. J. C. p. Saitoh, 2013, **98**, 1532-1539.
11. P. Zhang, D. Wan, Z. Zhang, G. Wang, J. Hu and G. J. E. S. N. Shao, 2018, **5**, 1813-1820.
12. Z. Xu, X. Li, K. Teng, B. Zhou, M. Ma, M. Shan, K. Jiao, X. Qian and J. J. J. o. M. S. Fan, 2017, **535**, 94-102.
13. L. Zhang, Y. He, L. Ma, J. Chen, Y. Fan, S. Zhang, H. Shi, Z. Li, P. J. A. a. m. Luo and interfaces, 2019, **11**, 34487-34496.
14. L. Huang, S. S. Manickam and J. R. J. J. o. m. s. McCutcheon, 2013, **436**, 213-220.
15. D. Miao, Z. Huang, X. Wang, J. Yu and B. Ding, *Small*, 2018, **14**, 10.